ChemComm

COMMUNICATION

View Article Online
View Journal | View Issue

Cite this: *Chem. Commun.*, 2018, **54**, 2142

Received 28th December 2017,
Accepted 2nd February 2018

DOI: 10.1039/c7cc09911h

rsc.li/chemcomm

Low-surface-area nitrogen doped carbon nanomaterials for advanced sodium ion batteries†

Chaokun Liu, Jiangtao Hu, Luyi Yang, Wenguang Zhao, Hejie Li and Feng Pan *

A low-surface-area nitrogen-doped carbon nanomaterial was prepared *via* a facile annealing method, which shows good Na-ion storage ability (334 mA g^{-1}) and coulombic efficiency due to its mixed charge–discharge mechanism and unique structural features.

Among various energy storage devices, rechargeable lithium-ion batteries (LIBs) are intensively studied as power sources for consumer portable electronic devices owing to their high specific capacity, rate capacity and cycling stability.[1,2] However, the high cost and limited terrestrial reserves of lithium may restrict LIBs' applications for large-scale energy storage.[3,4] Therefore, attention is starting to shift to exploring alternative energy storage technologies. Na-ion batteries (SIBs) have already become one of the most attractive low-cost alternatives to LIBs due to the abundant supply and wide distribution of sodium resources.[5] In recent years, significant progress has been made in the field of cathode materials for SIBs.[6,7] Correspondingly, several anode materials, such as metal oxides,[8,9] alloys,[10] and carbonaceous materials,[11] have also been investigated for SIBs. Since the first report on transition metal oxide spinel $NiCo_2O_4$ as an anode for SIBs in 2002,[8] many metal oxides such as Fe_2O_3,[12] SnO_2,[13] CO_2O_3[14] and CuO[15] have been investigated as anodes for SIBs. However, the relatively low initial coulombic efficiency, poor electronic conductivity, large hysteresis and enormous volume expansion have limited the application of metal oxides though they exhibit high capacity and energy densities.[16,17] Therefore, carbonaceous materials are regarded as the most promising candidates for SIBs due to their abundance, thermal stability and low price similar to anode materials for LIBs. However, graphite, which is used as the commercial LIB anode, exhibits an extremely low capacity of 31 mA h g^{-1} for Na-ion storage.[18] This is due to that in LIBs the formation of a series of binary graphite intercalation compounds (b-GICs) allows the reversible intercalation of Li-ions[19] while this mechanism cannot be applied to SIBs due to the lack of suitable binary intercalation compouds.[18] The mismatch between the Na ion and graphite structure leads to no existence of b-GICs under moderate conditions.[20,21] To overcome these issues, many other carbonaceous materials have been proposed, including hollow carbon nanowires/nanospheres,[22] carbon nanotubes (CNTs),[23] and porous carbon fibers, possessing a larger interlayer spacing with various morphologies and structures to obtain a higher capacity in Na-ion storage.[24] Introduction of nitrogen atoms is considered to be an effective way to improve the electrochemical performance of Na-ion batteries, which can enhance both the electric conductivity and capacity.[25,26] It is also reported that nitrogen doping can generate a pseudo-capacitance due to the interaction between the electrolyte and N species on the surface.[27] For example, Cao *et al.* investigated hollow carbon nanowires derived from polyaniline,[22] which can deliver a reversible capacity of 251 mA h g^{-1} with a 50.5% initial coulombic efficiency. Wang *et al.* synthesized porous N-doped nanosheets from graphene oxide (GO) that show a reversible capacity of 200 mA h g^{-1} after 250 cycles at a current density of 50 mA g^{-1}.[28] The studies described above have shown that N-doped porous carbon materials generally exhibit good rate and cycling capability, but the initial coulombic efficiency is typically very low due to the more prominent formation of a solid electrolyte interphase (SEI) layer on the large surface.[29] Therefore, a facile method for the synthesis of N-doped carbon with high capacity and a low surface area is desirable. Herein, we report a low-surface-area carbonaceous derivative of Prussian Blue (PB) with rich nitrogen doping, which can exhibit high reversible capacity (334 mA h g^{-1} at 0.05 A g^{-1}), excellent cycling performance (212 mA h g^{-1} after 200 cycles at the current density of 0.01 A g^{-1}) and a high initial coulombic efficiency of 64.9%. In addition, the different Na-ion storage mechanisms of the samples annealed at different temperatures have been discussed.

As demonstrated in Scheme 1, nitrogen doped carbon nanomaterials were synthesized *via* a facile annealing method using PB as a precursor (experimental details can be found in the ESI†). By applying different annealing temperatures (550 °C and 650 °C)

School of Advanced Materials, Peking University Shenzhen Graduate School, Shenzhen 518055, China. E-mail: panfeng@pkusz.edu.cn

† Electronic supplementary information (ESI) available: Experimental details; XPS data; kinetic analysis of CV. See DOI: 10.1039/c7cc09911h

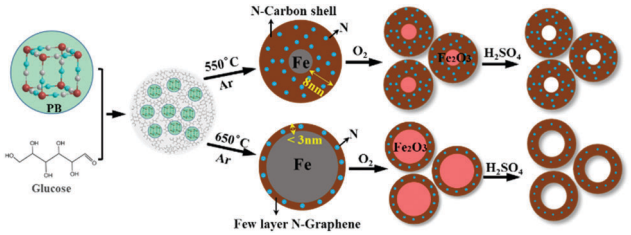

Scheme 1 Formation process of different nitrogen-doped hollow carbon shells (NC-550 and NC-650).

under an argon atmosphere, two types of nitrogen doped carbon (NC) can be obtained (NC-550 and NC-650).

The morphology and structure characteristics of NC-550 and NC-650 are investigated using scanning electron microscopy (SEM) and transmission electron microscopy (TEM). In the SEM image of NC-550 (Fig. 1a), it can be observed that NC-550 consists of blocky-shaped particles with diameters around 10–30 μm, which shows smooth surfaces with a few honeycomb-like structures exposed to the surface. However, as shown in Fig. 1d, NC-650 exhibits a much rougher surface indicating a porous structure. Images under higher magnification were taken to further investigate the crystalline structure of the samples. From the TEM images, NC-550 (Fig. 1b and c) clearly demonstrates that it has a relatively ordered macroporous feature with arranged thick graphene layers, which not only allows electrolyte permeation and but also enhances the sodium ion transfer rate between the electrode and the electrolyte.[29]

X-ray diffraction (XRD) patterns are collected to study the crystallinity information of the final two samples (Fig. 2a). Both NC-550 and NC-650 exhibit two broad peaks at around 25.8° and 43.0° on the XRD spectrum, which can be indexed to the (002) and (101) planes, respectively. Notably, N-550 shows a weak peak at 26.5°, indicating the presence of crystalline carbon or a graphite-like structure and a small d_{002} spacing of 0.34 nm. Compared to NC-650, NC-550 contains a more graphite-like domain which is transformed from graphene layers.[23] N_2 adsorption–desorption isotherms of NC-550 and NC-650 (Fig. 2b) both show typical type IV shapes with H_3 hysteresis, indicating the presence of mesopores.[25] NC-650 shows a high

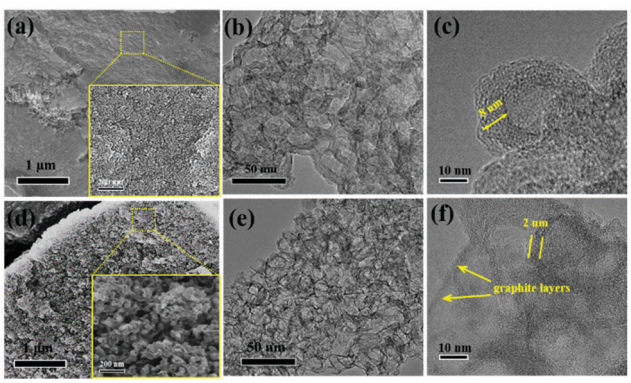

Fig. 1 SEM images of NC-550 (a) and NC-650 (d), and TEM images of NC-550 (b and c) and NC-650 (e and f).

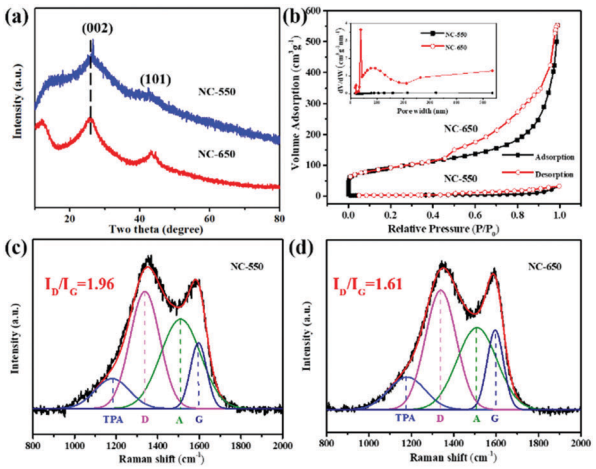

Fig. 2 (a) XRD data of NC-550 and NC-650; (b) N_2 adsorption/desorption isotherms of NC-550 and NC-650; and Raman spectra of N-550 (c) and NC-650 (d), which are fitted into four Lorentzian peaks.

Brunauer–Emmett–Teller (BET) surface area of 553.2 $m^2\ g^{-1}$, while NC-550 only shows a much lower specific surface area of 12.1 $m^2\ g^{-1}$.

According to the pore size distribution curves (Fig. 2b, inset), NC-550 mainly consists of macropores and a few mesopores and NC-650 shows a high content of mesopores, implying that the Fe^{3+} in PB has different catalytic effects on the formation of graphene layers at different temperatures. Furthermore, Raman spectra of NC-550 and NC-650 between 800 and 2000 cm^{-1} are measured to calculate the coherence lengths of graphenic domains (L_a) according to the following equation:

$$L_a(\mathrm{nm}) = (2.4 \times 10^{-10})\lambda_{\mathrm{nm}}{}^4 \left(\frac{I_G}{I_D}\right) \quad (1)$$

where λ_{nm} is 514 nm, and I_G and I_D are intensities of the G band and the D band, where the D band at ≈1350 cm^{-1} can be attributed to the A_{1g} vibration of finite-sized graphitic domains and the G-band at ≈1600 cm^{-1} is resulted from the E_{2g} vibration of sp^2 carbon.[26] Two broad peaks in the Raman spectra of NC-550 and NC-650 can be fitted into four Lorentzian peaks to identify the D and G bands accurately as shown in Fig. 2c and d. According to eqn (1), the L_a values of NC-550 and NC-650 are calculated to be 8.48 nm and 10.81 nm, respectively. The shorter coherence length of graphenic domains for NC-550 suggests that the graphenic layers in NC-550 may be shorter or more curved. Moreover, the ratio of I_D to I_G can also be considered as an indication of defect concentration.[30] Therefore, it can be deduced that NC-550 contains a higher concentration of defects due to a higher ratio (1.96) than that of NC-650 (1.61). It can be concluded that NC-550 has a lower degree of graphitization, which is reported to be advantageous in Na^+ storage.[31,32]

Recent studies have shown that nitrogen doping in carbon-based anodes plays an important role in the electrochemical performance of SIBs. Nitrogen dopants not only improve the electrical conductivity of carbon, but also generate extrinsic defects to support active Na storage sites.[25,26] X-ray photoelectron spectroscopy (XPS) measurements also were carried out to analyse

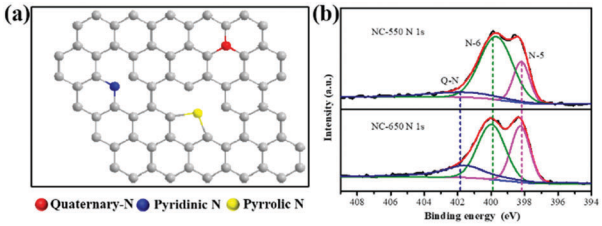

Fig. 3 (a) N 1s XPS survey spectra of NC-550 and NC-650 with fittings and (b) schematic of different types of N in carbon.

the different functional groups in NC-650 and NC-550 (shown in Fig. S1, ESI†). From Table S1 (ESI†) it can be seen that the atomic contents of nitrogen for NC-650 and NC-550 are 12.8% and 15.9%, respectively. The XPS data have been further analyzed, and XPS fitting was carried out for N 1s spectra. Fig. 3a shows three types of N atoms: pyridinic N (N-6), pyrrolic N (N-5) and quaternary N (N-Q). N-5 and N-6 are defective sites and usually considered to be electro-active for Na storage.[33] From Fig. 3b, it can be seen that the pyridinic N (N-6, 398.4 ± 0.2 eV) and pyrrolic N (N-5, 399.8 ± 0.2 eV) are dominant components in both samples. The total atomic contents of pyridinic and pyrrolic N in NC-550 and NC-650 are 90.5% and 77%, respectively. The higher content for defective N sites in NC-550 could be beneficial for its electrochemical performance.

To examine their electrochemical properties, NC-550 and NC-650 have also been fabricated into electrodes for Na-ion half-cells. Fig. 4a shows the first-cycle voltage profiles of NC-550 and NC-650 electrodes at the current density of 50 mA g^{-1}. The electrodes of NC-550 and NC-650 deliver reversible specific capacities of 373 and 292 mA h g^{-1} with initial coulombic efficiencies of 64.9% and 24.3%, respectively. The large irreversible capacity loss for NC-650 results from the large degree of electrolyte decomposition and SEI layer formation on its large surface, while NC-550 exhibits a higher initial coulombic efficiency and reversible capacity due to its unique structure with a low surface, more active sites and higher disorder degree for sodium storage. Fig. 4b displays the rate performances of the NC-550 and NC-650 electrodes. The NC-650 electrode exhibits a poor rate performance with a capacity of merely 110 mA h g^{-1} at a current density of 0.5 A g^{-1}, while the NC-550 electrode delivered reversible capacities of 334, 317, 295, 276, 247 and 212 mA h g^{-1} at current densities of 50, 80, 100, 150, 250, and 500 mA g^{-1}, respectively. And a reversible capacity of 315 mA h g^{-1} can be recovered as the current density reversed to 50 mA g^{-1}. In addition, as illustrated in Fig. 4c, a reversible capacity of 213 mA h g^{-1} (76.1% retention) was retained for the NC-550 electrode after 200 cycles at the density of 100 mA g^{-1}, which is twice that of NC-650 (93 mA h g^{-1}, 55.7% retention), so NC-550 exhibits a better capacity retention ratio with a slow capacity fading process compared with NC-650. After 200 cycles, a smaller charge-transfer impedance (R_{ct}) for NC-550 is demonstrated compared with NC-650 in the electrochemical impedance spectra (Fig. 4d), which is another evidence for less SEI formation on the NC-550 electrode. Fig. 4a–d show that NC-550 possesses superior electrochemical properties compared to NC-650, which

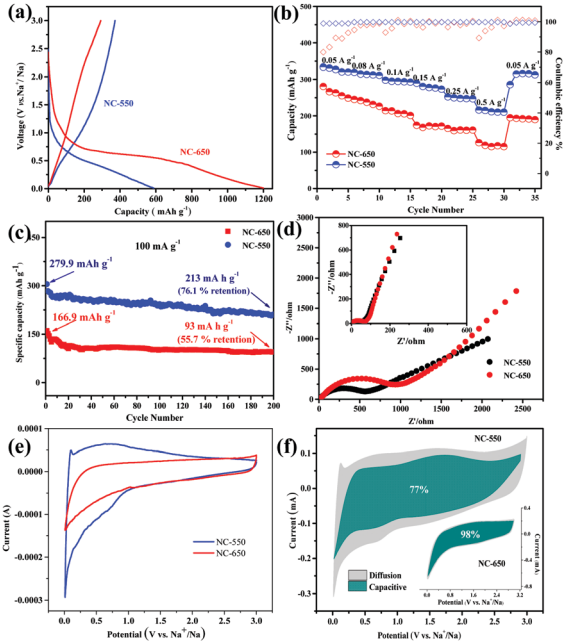

Fig. 4 (a) First-cycle voltage profiles of two samples at a current rate of 50 mA g^{-1}; (b) cycling performances of NC-550 and NC-650 at different densities; (c) long-term cycling performances of NC-550 and NC-650; (d) Nyquist plots of half cells with NC-550 and NC-650 before (inset) and after 200 cycles; (e) 2nd cyclic voltammograms of half cells at the scan rate of 0.1 mV s^{-1}; and (f) capacitive charge storage contributions of NC-550 and NC-650 at the scan rate of 1 mV s^{-1}.

can be attributed to its unique structures demonstrated above including the lower specific surface area, lower degree of graphitization and more active N-doping sites. Since NC-550 and NC-650 exhibit varied voltage profiles (Fig. S2, ESI†), it is of great importance to study their charge–discharge mechanisms.

The cyclic voltammetry (CV) results of NC-550 and NC-650 are shown in Fig. 4e. It can be seen that during the anodic scan, NC-550 shows a sharp desodiation peak, which is observed for NC-650, suggesting that the charge–discharge mechanisms for NC-550 and NC-650 might be different. Generally, the current collected from the carbon-based anodes includes a redox pseudo capacitive process generated at the surface of active materials and the diffusion-controlled process in the bulk of materials.[34] To further study the pseudo capacitance's contribution to the total Na-ion storage, CV curves at different current densities were applied. The contribution from capacitive effects and the diffusion-controlled process can be represented as:

$$i(V) = k_1\nu + k_2\nu^{1/2} \quad (2)$$

where $i(V)$ represents the total current response at a given potential V, ν is the scan rate, and k_1 and k_2 are constants. Here, $k_1\nu$ and $k_2\nu^{1/2}$ correspond to the surface capacitive behaviour and the diffusion-controlled process, respectively. After interpreting the results from CV curves at different scan rates (details shown in Fig. S3 and S4, ESI†), the values of k_1 and k_2 can be determined in order to calculate the pseudo capacitive current contribution at a given potential. As shown in Fig. 4f, at the scan rate of 1 mV s^{-1}, the potential profiles for the current

responses of capacitive effects are presented to compare with the total measured current area. A dominating capacitive contribution is 98% for a NC-650 electrode, indicating that the Na-ion storage is significantly associated with the surface reaction. However, the NC-550 electrode delivers a smaller pseudo capacitance storage (77%), indicating that the Na-ion storage is only partly related with the surface reaction. To understand the kinetic origin, the degree of capacitive effect can be qualitatively analysed corresponding to the relationship between the measured current (i) and scan rate (ν) from the CV curves:

$$i = a\nu^b \quad (3)$$

where a and b are both constants. The value of b, generally found between 0.5 (diffusion limited) and 1.0 (surface capacitance-dominated), is determined from the slope of the log(i) *vs.* log(ν) curve (details shown in Fig. S5, ESI†). The b-values of NC-550 at different potentials are in between 0.5 and 1, indicating a mixture of both the lithium semi-innate linear diffusion and the surface reaction. In contrast, the b-values of NC-650 are approximately 1 at all potentials, indicating that the surface reaction contributes almost 100% capacity of NC-650 due to its large surface area. As a result, it is believed that this mixed Na^+ storage mechanism of NC-550, which originates from its unique structure, is the main reason for the improved electrochemical performances.

To conclude, carbon nanosheets with relatively low specific surface areas (NC-550) and high specific surface areas (NC-650) were prepared and tested as anode materials for SIBs. NC-550 exhibits high initial coulombic efficiency (64.9%), reversible capacity (334 mA h g^{-1} at 50 mA g^{-1}) and excellent cycling performance (212 mA h g^{-1} after 200 cycles at 100 mA g^{-1}). The superior electrochemical properties of NC-550 can be attributed to its mixed charge–discharge mechanism and structural features including the lower specific surface area, lower degree of graphitization and more active N-doping sites. This promising approach can be further explored to acquire low-cost materials for sodium-ion batteries.

This work was financially supported by the National Materials Genome Project (2016YFB0700600), the National Natural Science Foundation of China (51602009), and the Guangdong Innovation Team Project (2013N080).

Conflicts of interest

There are no conflicts to declare.

Notes and references

1 B. Dunn, H. Kamath and J.-M. Tarascon, *Science*, 2011, **334**, 928–935.
2 B. Scrosati, J. Hassoun and Y.-K. Sun, *Energy Environ. Sci.*, 2011, **4**, 3287.
3 S. W. Kim, D. H. Seo, X. Ma, G. Ceder and K. Kang, *Adv. Energy Mater.*, 2012, **2**, 710–721.
4 M. D. Slater, D. Kim, E. Lee and C. S. Johnson, *Adv. Funct. Mater.*, 2013, **23**, 947–958.
5 D. A. Stevens and J. R. Dahn, *J. Electrochem. Soc.*, 2001, **148**, A803–A811.
6 M. H. Han, E. Gonzalo, G. Singh and T. Rojo, *Energy Environ. Sci.*, 2015, **8**, 81–102.
7 M. S. Islam and C. A. J. Fisher, *Chem. Soc. Rev.*, 2014, **43**, 185–204.
8 R. Alcántara, M. Jaraba, P. Lavela and J. L. Tirado, *Chem. Mater.*, 2002, **14**, 2847–2848.
9 Y. Sun, L. Zhao, H. Pan, X. Lu, L. Gu, Y. S. Hu, H. Li, M. Armand, Y. Ikuhara, L. Chen and X. Huang, *Nat. Commun.*, 2013, **4**, 1810–1870.
10 S. J. R. Prabakar, Y. H. Hwang, E. G. Bae, S. Shim, D. Kim, M. S. Lah, K. S. Sohn and M. Pyo, *Adv. Mater.*, 2013, **25**, 3307–3312.
11 C. Zhu, X. Mu, P. A. Vanaken, Y. Yu and J. Maier, *Angew. Chem., Int. Ed.*, 2014, **53**, 2152–2156.
12 S. Komaba, T. Mikumo, N. Yabuuchi, A. Ogata, H. Yoshida and Y. Yamada, *J. Electrochem. Soc.*, 2010, **157**, A60.
13 D. Su, X. Xie and G. Wang, *Chem. – Eur. J.*, 2014, **20**, 3192–3197.
14 M. M. Rahman, A. M. Glushenkov, T. Ramireddy and Y. Chen, *Chem. Commun.*, 2014, **50**, 5057–5060.
15 L. Wang, K. Zhang, Z. Hu, W. Duan, F. Cheng and J. Chen, *Nano Res.*, 2014, **7**, 199–208.
16 Y. H. Chao, J. S. Wu, C. E. Wu, J. F. Jheng, C. L. Wang and C. S. Hsu, *Adv. Energy Mater.*, 2013, **3**, 1279–1285.
17 Y. Zhu, X. Han, Y. Xu, Y. Liu, S. Zheng, K. Xu, L. Hu and C. Wang, *ACS Nano*, 2013, **7**, 6378–6386.
18 B. Jache and P. Adelhelm, *Angew. Chem., Int. Ed.*, 2014, **53**, 10169–10173.
19 G. Schmuelling, T. Placke, R. Kloepsch, O. Fromm, H. W. Meyer, S. Passerini and M. Winter, *J. Power Sources*, 2013, **239**, 563–571.
20 K. Nobuhara, H. Nakayama, M. Nose, S. Nakanishi and H. Iba, *J. Power Sources*, 2013, **243**, 585–587.
21 J. Sangster, *J. Phase Equilib. Diffus.*, 2007, **28**, 571–579.
22 Y. Cao, L. Xiao, M. L. Sushko, W. Wang, B. Schwenzer, J. Xiao, Z. Nie, L. V. Saraf, Z. Yang and J. Liu, *Nano Lett.*, 2012, **12**, 3783–3787.
23 I. Elizabeth, R. B. Mathur, P. H. Maheshwari, B. P. Singh and S. Gopukumar, *Electrochim. Acta*, 2015, **176**, 735–742.
24 W. Luo, Z. Jian, Z. Xing, W. Wang, C. Bommier, M. M. Lerner and X. Ji, *ACS Cent. Sci.*, 2015, **1**, 516–522.
25 H. Wang, C. Zhang, Z. Liu, L. Wang, P. Han, H. Xu, K. Zhang, S. Dong, J. Yao and G. Cui, *J. Mater. Chem.*, 2011, **21**, 5430.
26 W. H. Shin, H. M. Jeong, B. G. Kim, J. K. Kang and J. W. Choi, *Nano Lett.*, 2012, **12**, 2283–2288.
27 Y. Wu, S. Fang and Y. Jiang, *J. Mater. Chem.*, 1998, **8**, 2223–2227.
28 F. Su, C. K. Poh, J. S. Chen, G. Xu, D. Wang, Q. Li, J. Lin and X. W. Lou, *Energy Environ. Sci.*, 2011, **4**, 717–724.
29 H. G. Wang, Z. Wu, F. L. Meng, D. L. Ma, X. L. Huang, L. M. Wang and X. B. Zhang, *ChemSusChem*, 2013, **6**, 56–60.
30 C. Hu, S. Sedghi, A. Silvestre-Albero, G. G. Andersson, A. Sharma, P. Pendleton, F. Rodríguez-Reinoso, K. Kaneko and M. J. Biggs, *Carbon*, 2015, **85**, 147–158.
31 C. Bommier, T. W. Surta, M. Dolgos and X. Ji, *Nano Lett.*, 2015, **15**, 5888–5892.
32 B. Cao, H. Liu, B. Xu, Y. Lei, X. Chen and H. Song, *J. Mater. Chem. A*, 2016, **4**, 6472–6478.
33 H. Liu, M. Jia, B. Cao, R. Chen, X. Lv, R. Tang, F. Wu and B. Xu, *J. Power Sources*, 2016, **319**, 195–201.
34 W. Ren, K. Wang, J. Yang, R. Tan, J. Hu, H. Guo, Y. Duan, J. Zheng, Y. Lin and F. Pan, *J. Power Sources*, 2016, **331**, 232–239.